Article

Relevance of Sulfate Functionalization and Porous Structure of TiO₂ Ceramic Foams in Photocatalytic Degradation of Dye Molecules

Paula G. P. Moraes, [a] *Marinalva A. Alves-Rosa,* [a] *Celso V. Santilli* [a] *and Sandra H. Pulcinelli* *,[a]

ᵃInstituto de Química, Universidade Estadual Paulista (UNESP), Rua Prof. Francisco Degni, 55,
14800-060 Araraquara-SP, Brazil

A one-step route was developed for sulfate functionalization of titania foam, consisting of integrating the sol-gel process with an emulsion template. The resulting material was used to evaluate the relevance of the porous structure and surface sulfate groups in the photocatalytic degradation of Rhodamine B molecules in water under UV irradiation. X-ray diffraction (XRD) analysis showed that the anatase crystalline phase was metastabilized by functionalization of the surface with sulfate species, which caused the crystallite size to decrease from 21 to 10 nm, while the specific surface area increased from 4 to 42 cm² g⁻¹. Small-angle X-ray scattering (SAXS) measurements during heating of the non-sulfated (E-TiO₂) and sulfated (E-TiO₂/SO₄²⁻) sols emulsified with sodium dodecyl sulfate (SDS) as surfactant and isopropyl myristate as the nonpolar phase, revealed formation of the liquid crystalline structure. Elimination of this mesophase template allowed the preparation of ceramic foams with hierarchical structure formed by meso- and macropore families. The kinetics of photodegradation reaction of Rhodamine B followed a pseudo-first order mechanism. The most efficient photocatalytic activity (higher rate constant and shorter half-life time) was obtained for the foam templated using 20% of SDS (E-TiO₂/SO₄²⁻ 20SDS), which exhibited the highest values for porosity (93%) and specific surface area (80 m³ g⁻¹).

Keywords: sulfated titania, sol-gel, emulsion template, ceramic foam, dye photodegradation

Introduction

Titanium dioxide is a broadband semiconductor that presents attractive features such as nontoxicity and low cost, as well as photo- and chemical stability.[1] Different crystalline structures may be present, including the rutile phase, which is thermodynamically stable at around room temperature, and the anatase and brookite phases, which are metastable and change to the rutile structure at temperatures between 600 and 700 °C.[2,3] The rutile and anatase structures have been most widely studied and are distinguished by the distortion of the Ti^{4+} octahedra and the ways that they are connected, with zigzag and linear chains in anatase and rutile, respectively.[1,2]

Heterogeneous photocatalysis is an important application of TiO₂, where the anatase polymorph is considered to present the best photoactivity,[2-4] mainly related to properties such as the crystallite size, surface area, and porous structure. Heterogeneous photocatalysis, which involves the activation of a solid semiconductor by irradiation with sunlight or artificial light, is a promising technique for the oxidation of organic contaminants, focusing on environmental remediation.[5-8] Among the ways that have been studied for improving the photocatalytic activity of TiO₂, sulfation has proved to be a simple and efficient method.[9] The modification of titanium dioxide with sulfate ions has led to greater photocatalytic activity in the degradation reactions of toluene, hexane, phenol, trichloroethylene, and some dyes.[3,9-14] This is because the modification stabilizes the anatase phase and increases the surface area after high-temperature calcination treatment. Furthermore, the presence of surface acid sites on the sulfated TiO₂ can increase the adsorption of organic pollutants and provide more efficient capture of photoinduced electrons, consequently increasing the quantum yield. Sulfate groups increase the acidity of this oxide by the formation of Brønsted and Lewis sites in the structure, with the S=O groups acting in the removal of electron species, increasing the acid strength of the metal cations (Ti^{4+}) by inductive effects.[15-17]

*e-mail: sandra.h.pulcinelli@unesp.br

Sulfated oxide catalysts are usually prepared by impregnation of sulfate groups on metal oxides.[3,18] The aim of the present study was to develop a new process that combined the formation of TiO$_2$ particles and sulfation in a single step, employing the sol-gel method. The resulting sulfated TiO$_2$ colloidal suspension was used as a continuous phase emulsion template, according to the strategy for the production of porous ceramics with hierarchical structure.[19,20] Subsequently, gelation of the suspension occurred around oil droplets. As a result, micelles formed only by surfactant molecules or the oil droplets dispersed in the colloidal suspension could template the mesopores and macropores, respectively, obtained after heat treatment. This hierarchical organization of pores is important, because macropores facilitate the diffusion of reagents and products, while mesopores increase the surface area, promoting the existence of more active sites for the catalytic reactions.[20]

Therefore, the objective of this work was to prepare porous titania ceramics with hierarchical structures of pores by integration of the sol-gel process and the use of emulsions as pore templates. Evaluation was then made of the effect of the simultaneous synthesis and sulfation of TiO$_2$ on the porous characteristics and photocatalytic activity of the resulting material.

Experimental

Chemicals

All the chemicals used in this work, including titanium tetraisopropoxide (Ti(O^{i}Pr)$_4$, C$_{12}$H$_{28}$O$_4$Ti, 99%, CAS 546-68-9), *p*-toluene sulfonic acid (PTSH, CH$_3$C$_6$H$_4$SO$_3$H, PA, CAS 6192-52-5), isopropanol ((CH$_3$)$_2$CHOH, 90%, CAS 67-63-0), nitric acid (HNO$_3$, 90%, CAS 7697-37-2), sodium dodecyl sulfate (SDS, C$_{12}$H$_{25}$O$_4$S.Na, 99%, CAS 151-21-3), and isopropyl myristate (C$_{17}$H$_{34}$O$_2$, PA, CAS 110-27-0), were purchased from Sigma-Aldrich (Merck, São Paulo, Brazil) and were used as received.

Preparation of the porous titania

The alcohol sol was obtained according to the route previously described by Kaminski *et al.*,[21] where an acidic aqueous solution of *p*-toluene sulfonic acid (PTSH) was added dropwise to a solution of Ti(O^{i}Pr)$_4$ in isopropanol (2 mol L^{-1}), under an inert atmosphere and with magnetic stirring. The hydrolysis ratio (H = [H$_2$O]/[Ti]) was fixed at 1.5. An acid-catalyzed sol-gel method was used, where the molar acidity ratio (A = [acid]/[Ti]) was fixed at 1 for the TiO$_2$/SO$_4^{2-}$ suspensions, in which PTSH acted as

catalyst as well as sulfate source for the functionalization. For comparison, a non-sulfated TiO$_2$ reference sample was prepared under similar conditions, using an aqueous solution of nitric acid (HNO$_3$), instead of PTSH. The nomenclature of the samples was compiled at Table 1.

Table 1. Samples nomenclature taking account for the acid nature, the acidity ratio, and the quantity of sodium dodecyl sulfate (surfactant) and isopropyl myristate (oil)

Sample	Acid	H$^+$/Ti	Surfactant / %	Oil / %
TiO$_2$	HNO$_3$	1	0	0
TiO$_2$/SO$_4^{2-}$	PTSH	1	0	0
E-TiO$_2$/SO$_4^{2-}$	HNO$_3$	1	20	40
E-TiO$_2$/SO$_4^{2-}$20SDS	PTSH	1	20	40
E-TiO$_2$/SO$_4^{2-}$30SDS	PTSH	1	30	40

PTSH: *p*-toluene sulfonic acid.

The emulsions were prepared under vigorous stirring, using the TiO$_2$/SO$_4^{2-}$ sol as the polar phase, SDS as surfactant, and isopropyl myristate as the nonpolar phase. Gelation of the emulsion was promoted by the addition of water, followed by aging for 5 days, drying at room temperature, and thermal treatment at 600 °C for 2 h. The samples were also submitted to a water washing procedure to eliminate the Na$_2$SO$_4$ formed from the SDS.

Characterization

The crystalline phases in the calcined samples were studied by X-ray diffraction (XRD), using a Siemens D5000 diffractometer (Siemens, Karls-ruhe, Germany), with Cu Kα radiation selected by a curved graphite monochromator, and scanning in the range 10° ≤ 2θ ≤ 80°. The average crystallite size (D) was estimated from the XRD peak using the Scherrer equation:[22] D = kλ/βcosθ, where k is the shape constant, λ is the X-ray wavelength, θ is the diffraction angle, and β is the full-width-at-half-maximum (FWHM) of the diffraction peak, corrected for instrumental broadening.

Fourier transform infrared spectroscopy (FTIR) measurements were performed using a Bruker VERTEX 70 instrument (Bruker, Germany) operated in attenuated total reflection mode (ATR-FTIR). Spectra were acquired in the range from 4000 to 400 cm^{-1}, with resolution of 4 cm^{-1} and 64 scans. Ultraviolet-visible diffuse reflectance spectroscopy (UV-Vis DRS) experiments were performed in the range 200-800 nm, using a Varian Cary 500 Scan spectrophotometer (Agilent Technologies, Santa Clara, CA, USA) equipped with an integrating sphere. The Kubelka-Munk function[23,24] was used to convert the diffuse reflectance spectra to the corresponding UV-Vis absorption

spectra. The bandgap energy values were calculated from the UV-Vis data using the Tauc equation: $\alpha h\nu = A(h\nu - E_g)^n$, where $h\nu$ is the incident photon energy, α is the absorption coefficient, A is a constant, E_g is the bandgap energy, and n depends on the nature of transition, with values of 1/2 and 2 for direct and indirect transitions, respectively.

The thermal behaviors of the dried samples were investigated by simultaneous thermogravimetric analysis (TGA) and differential thermal analysis (DTA), performed from room temperature up to 1000 °C, in a static air atmosphere, using a SDT600 system (TA Instruments, New Castle, DE, USA) operated at a heating rate of 5 °C min⁻¹.

Small-angle X-ray scattering (SAXS) measurements of the dried emulsion gels were performed at the SAXS1 beamline of the National Synchrotron Light Laboratory (LNLS, Campinas, Brazil). This beamline was equipped with a silicon (111) monochromator (λ = 1.549 Å), a vertical detector localized 1000 mm from the sample, and a multichannel analyzer to record the scattering intensity, I(**q**), as a function of the scattering vector, **q**. *In situ* SAXS measurements were carried out during the programmed change of temperature. The samples were placed in quartz capillaries and heated from room temperature to 450 °C, at a rate of 5 °C min⁻¹, in a LINKAM THMS600 furnace. The interplanar distances (d) were calculated using $d = 2\pi/\mathbf{q}$.[25]

Nitrogen adsorption-desorption isotherms were recorded at liquid nitrogen temperature, in the relative pressure interval between 0.001 and 0.998, using an ASAP 2010 instrument (Micromeritics, Norcross, GA, USA). The samples were degassed at 200 °C for 12 h under vacuum of 10 μPa. The surface areas were calculated using the Brunauer-Emmett-Teller (BET) equation.[26] The pore size distribution was determined by mercury intrusion porosimetry, using an AUTOPORE III instrument (Micromeritics, Norcross, GA, USA). Before analysis, the samples were degassed at pressure below 50 μPa. The pore diameter was calculated using the Washburn equation.[27] The porous structure was examined by scanning electron microscopy, using a Philips XL 30 FEG instrument (Philips, Leuven, Belgium). The calcined samples were deposited on aluminum sample holder and sputtered with carbon.

Photocatalytic assay

The photocatalytic activities of the samples were evaluated in the degradation reaction of Rhodamine B dye (RhB). A continuous type reactor was used in a dark box equipped with a low power (15 W) germicidal lamp emitting radiation at a wavelength of around 254 nm.

A 100 mg portion of the photocatalyst was dispersed in 25 mL of aqueous RhB solution (25 mg L⁻¹). This suspension was magnetically stirred for 1 h, in the dark, to achieve adsorption/desorption equilibrium among the photocatalyst, the dye, and dissolved oxygen. The lamp was then positioned 6 cm from the surface of the RhB solution. During the degradation, aliquots were removed at regular time intervals, filtered, and the filtrate was analyzed by UV-Vis spectroscopy at 553 nm (λ_{max}). The kinetic parameters of the degradation reaction were determined considering a pseudo-first order reaction.

Results and Discussion

The effect on its thermal stability of foaming the sulfated titania with increasing amounts of surfactant (SDS) was evaluated from the TGA and DTA curves (Figure 1). The non-foamed material presented three main mass loss steps: an initial endothermic evaporation of adsorbed molecules (water and isopropanol) below 200 °C; a second step, between around 300 and 450 °C, corresponding to an exothermic process associated with the elimination of non-dissociated PTSH molecules and other organic compounds; and a third step, at 500-650 °C, related to exothermic decomposition of PTSH molecules linked to the TiO₂ surface. The foaming with nonpolar liquid and SDS led to strong decreases of the evaporation of physically adsorbed molecules, which were probably replaced by SDS molecules. The SDS solution, used as a soft pores template, was lost in two main steps between 150 and 500 °C. The most important mass loss occurred near the boiling point temperature (ca. 180 °C) of the isopropyl myristate, while the strongly bonded sulfate species were probably responsible for the mass loss observed above.[11] However, the evolution of the number and intensity of exothermic maxima observed in this temperature range evidenced the complexity of the phenomena occurring during formation of the gas foam by thermal elimination of the soft template. As the thermal analysis of TiO₂/SO₄²⁻ showed that the practical elimination of adsorbed sulfate species occurs at temperatures above 700 °C, the standard calcination temperature of the ceramic materials was fixed at 600 °C to preserve the particular surface and structural features of sulfated samples. The endothermic events at around 875 °C, with no mass losses, observed for samples containing 20 and 30% of SDS, were related to the fusion of Na₂SO₄ originated from the SDS surfactant.[28]

The X-ray diffractograms for the calcined sulfated titania, non-foamed and foamed with SDS solution, showed the main Bragg reflections of the anatase phase (JCPDS card 21-1272), while the diffractogram for the
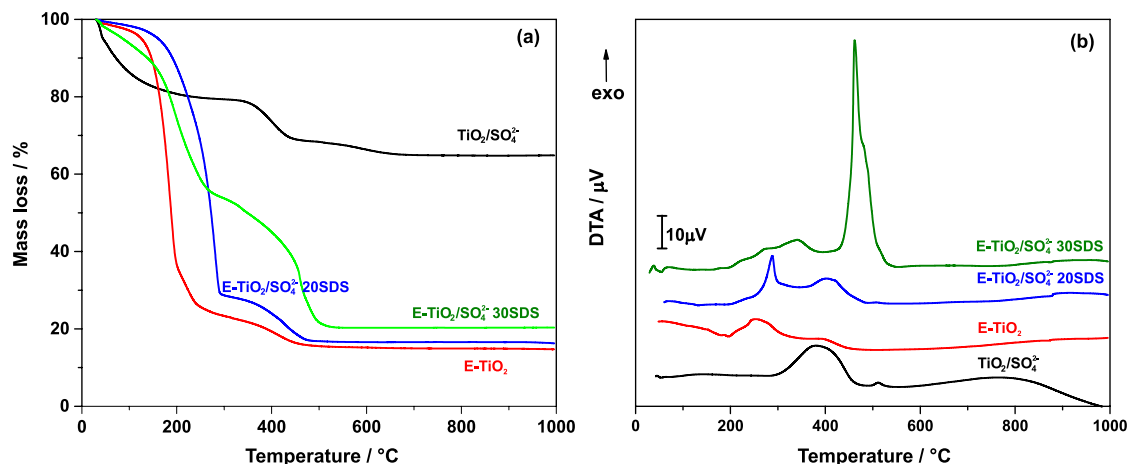
Figure 1. TGA (a) and DTA (b) curves for non-foamed sulfated titania (TiO₂/SO₄²⁻) and foamed non-sulfated titania (E-TiO₂) and foamed sulfated titania prepared using 20 and 30% of SDS (E-TiO₂/SO₄²⁻ 20SDS and E-TiO₂/SO₄²⁻ 30SDS).

non-sulfated titania showed a mixture of anatase and rutile (JCPDS card 21-1276) phases (Figure 2). Irrespective of the SDS amount, the presence of PTSH promoted stabilization of the anatase phase and induced a reduction of the average crystallite size of the titania from 21 to 10 nm, with consequent increase of the specific surface area from 2 to 42 cm² g⁻¹. Scolan and Sanchez[29] related this phenomenon to a solvating layer involving species based on PTSH and water molecules, which surrounded the TiO₂ nanoparticles. In addition, sulfate groups from PTSH could be linked to the titanium octahedra, suppressing the growth of linear chains along the edges, consequently inhibiting formation of the rutile phase and retarding crystallite growth.[3,4,13,14]
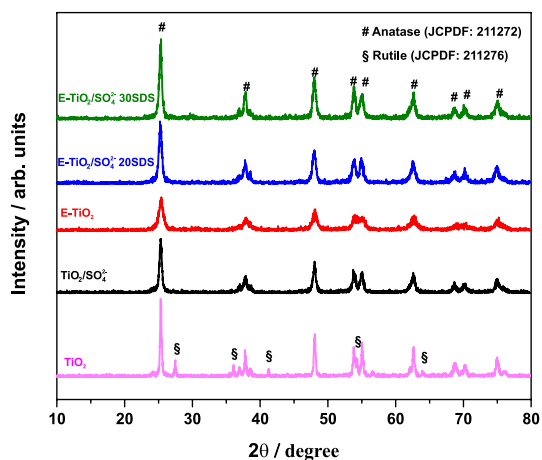
Figure 2. X-ray diffractograms of the calcined non-foamed non-sulfated and sulfated titania (TiO₂ and TiO₂/SO₄²⁻), the foamed non-sulfated (E-TiO₂) and the foamed sulfated titania with 20% (E-TiO₂/SO₄²⁻ 20SDS) and 30% (E-TiO₂/SO₄²⁻ 30SD) of SDS.

The octahedral symmetry of TiO₆ was evident from the infrared spectra (Figure 3). Irrespective of the presence of SDS, the spectra of the sulfated titania presented a set of bands in the range 1250-1000 cm⁻¹, attributed to S–O and

S=O stretching vibrations of uni- and bidentate sulfate coordinated to Ti.[30] Finally, the presence of a sulfate band in the sample prepared in the absence of PTSH (E-TiO₂) clearly evidenced the participation of the SDS molecules as sulfating agents, modifying the surface properties of the TiO₂ nanoparticles.
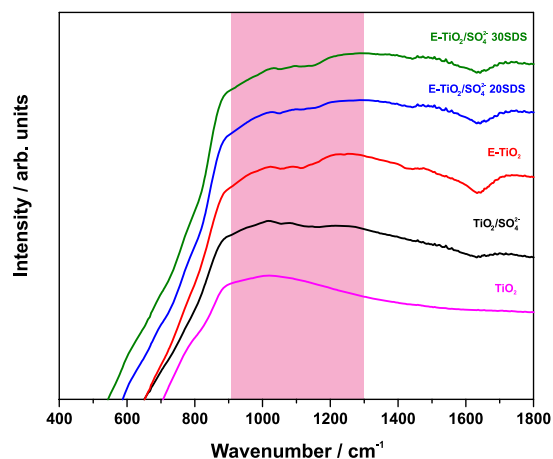

Figure 3. Infrared spectra (FTIR-ATR) of the calcined non-foamed non-sulfated and sulfated titania (TiO₂ and TiO₂/SO₄²⁻), the foamed non-sulfated (E-TiO₂) and the foamed sulfated titania with 20% (E-TiO₂/SO₄²⁻ 20SDS) and 30% (E-TiO₂/SO₄²⁻ 30SD) of SDS.

The temperature-dependent SAXS curves acquired during *in situ* heating of the xerogels prepared with non-sulfated titania and sulfated titania, foamed using different amounts of SDS (Figure 4), showed thin and intense peaks characteristic of diffraction by periodic arrangements of the mesophase. In this case, the crystallographic structure could be determined using the positions of the Bragg peaks. The relationship between the Bragg peak positions in the reciprocal space is given by q ratios (q_1/q_1:q_2/q_1:q_3/q_1, and so on) of 1:2:3:4, etc., for the lamellar arrangement of mesophases, and of 1:$\sqrt{3}$:2:$\sqrt{7}$, etc., for

the hexagonal ones. The cubic phases present five groups of symmetry, each one characterized by specific relations between the **q** values of the Bragg peaks.[25,31,32] Below 130 °C, the position ratios of the three peaks observed for the non-sulfated E-TiO$_2$ mesophase (Figure 4a) were equal to 1:2:3, characterizing the presence of a lamellar phase (L$_1$). Above this temperature, two new diffraction peaks grew, at the expense of the L$_1$ peaks, which were no longer observed above 170 °C. The upshift of the two new peaks hindered the experimental observation of the third peak. Nevertheless, the two new peak positions also presented q ratios of 1:2, indicating the formation of an independent lamellar phase (L$_2$). This L$_1$→L$_2$ lamellar mesophase transformation occurred near the isopropyl myristate mass loss, while the disappearance of L$_2$ occurred near the end (220 °C) of this stage of mass loss (Figure 1). At higher temperatures, no more diffraction peaks were observed in the SAXS curves, indicating a loss of periodic order of the mesophase structure. The main difference between the L$_1$ and L$_2$ phases was the organization of the carbon chains of the nonpolar phase and of the surfactant

in the bilayers. It should be noted that the interlamellar distance decreased from 3.90 to 3.34 nm, for L$_1$ and L$_2$, respectively, as the temperature increased. This shrinkage could be attributed to a transition from a fluid-like to a solid-like state, due to the increase of the SDS concentration with evaporation of the isopropyl myristate.

For the mesophase obtained using 20% SDS (Figure 4b) the first diffraction peak occurred at higher **q** values, corresponding to an interlamellar distance of the order of 1.8 nm, indicating that the structure became more compacted. The diffraction peaks were present up to temperatures as high as 400 °C, demonstrating the higher thermal stability of the mesophases. A notable feature was that as the temperature increased, some peaks appeared, while others disappeared, characteristic of the presence of mixtures and/or transitions between different phases. Peaks related by the ratio 1:2, characteristic of lamellar mesophases, only appeared after 240 and 280 °C, with interlamellar distances reaching 2.32 and 2.82 nm, indicating that an expansion of the lamellar structure occurred with increase of the temperature. Above 400 °C,
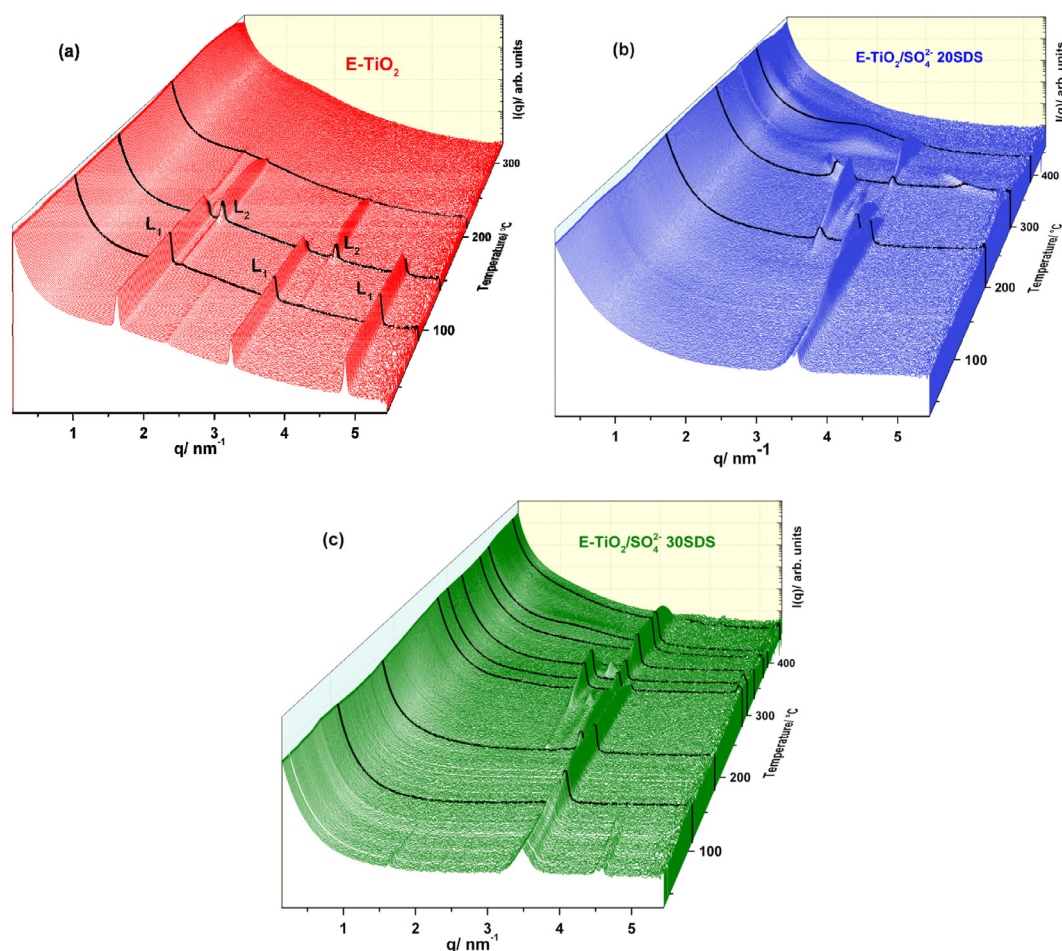
Figure 4. Evolution of SAXS curves, according to temperature, for the non-sulfated titania foamed with liquid containing 20% of SDS ((a) E-TiO$_2$) and for the sulfated titania foamed with liquid containing 20% ((b) E-TiO$_2$/SO$_4^{2-}$ 20SDS) and 30% ((c) E-TiO$_2$/SO$_4^{2-}$ 30SD) of SDS.

*J. Braz. Chem. Soc.* **2024**, *35*, 11, e-20240088

5 of 10

the diffraction peaks disappeared, indicating that the lamellar structure was lost, in good agreement with the TGA/DTA results (Figure 1), reflecting the elimination of SDS and formation of the anatase phase at this temperature. Hence, the extraction of the surfactant molecules that formed the micelles, together with the tensions associated with crystallization and crystallite growth, could have been responsible for collapse of the mesophase.

The SAXS curves for the sample obtained using 30% SDS (Figure 4c) showed the presence of peaks different from those observed before, but with similar thermal evolution. The results evidenced that the porous template structure (form, size, and volume of the pores) had been modified. The first diffraction peak indicated an interlamellar distance of 1.81 nm, while this increased to 2.3 nm for temperatures up to 200 °C. However, the main difference observed with increase of the surfactant amount was the higher temperature at which the order of the mesophase was lost, characterized by the diffraction peak vanishing at 457 °C. It could be concluded that increase of the SDS amount favored the mesophase structure, enabling it to be maintained at higher temperatures. This could be explained by improvement of the nonpolar interaction (phase-surfactant-aqueous phase) that acted as a structuring agent for organization of the surfactant molecules on the walls of the titania mesophases.[33]

The effect of surfactant addition on the microstructure of titania samples was observed by scanning electron microscopy (SEM) and the micrograph are displayed at Figure 5. Globular primary aggregates, which packaging originates pores with irregular size and shape, are observed for the all samples. The primary aggregates observed for the non-foamed TiO$_2$/SO$_4^{2-}$ powder were larger (Figure 5a) than that observed for the foamed samples (Figures 5b and 5c), indicating that SDS surfactant difficult particles agglomeration and may be acting against sintering. The walls of the bigger pores templated by the emulsion are formed by secondary porous aggregates of ill-defined size and shape.
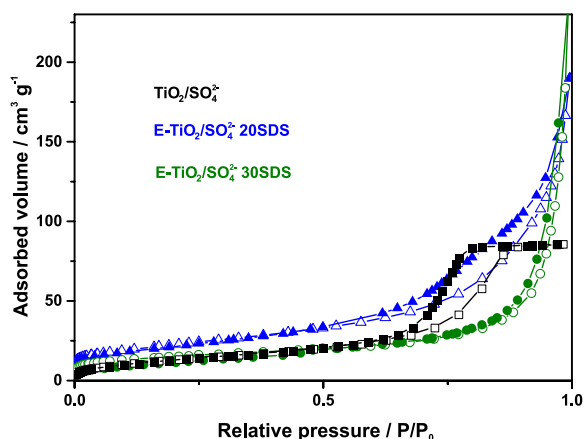
The changes in the porous textures of the non-foamed and foamed sulfated titania samples calcined at 600 °C were analyzed using mercury intrusion porosimetry and nitrogen adsorption isotherms. The main characteristics are summarized in Table 2. Figure 6 shows the N$_2$ adsorption-desorption isotherms for the non-foamed sulfated titania and the sulfated titania foamed with 20 and 30% of SDS. The non-foamed sample (TiO$_2$/SO$_4^{2-}$) exhibited type IV isotherm and type H1 hysteresis loop, attributed to the mesopores formed by agglomerates of spheroidal particles of fairly uniform size and array.[26] The absence of the plateau a high relative pressure (P/P$_0$ ca. 1) at the adsorption curve of samples foamed with 20 and 30% of SDS is characteristic of type II isotherm associated to the presence of macropores (size > 50 nm), in good agreement with the size evidenced by SEM images. The H3 hysteresis lop observed for the E-TiO$_2$/SO$_4^{2-}$ 20SDS sample is characteristic of slit-shaped pores formed by plate-like particles, which is consistent
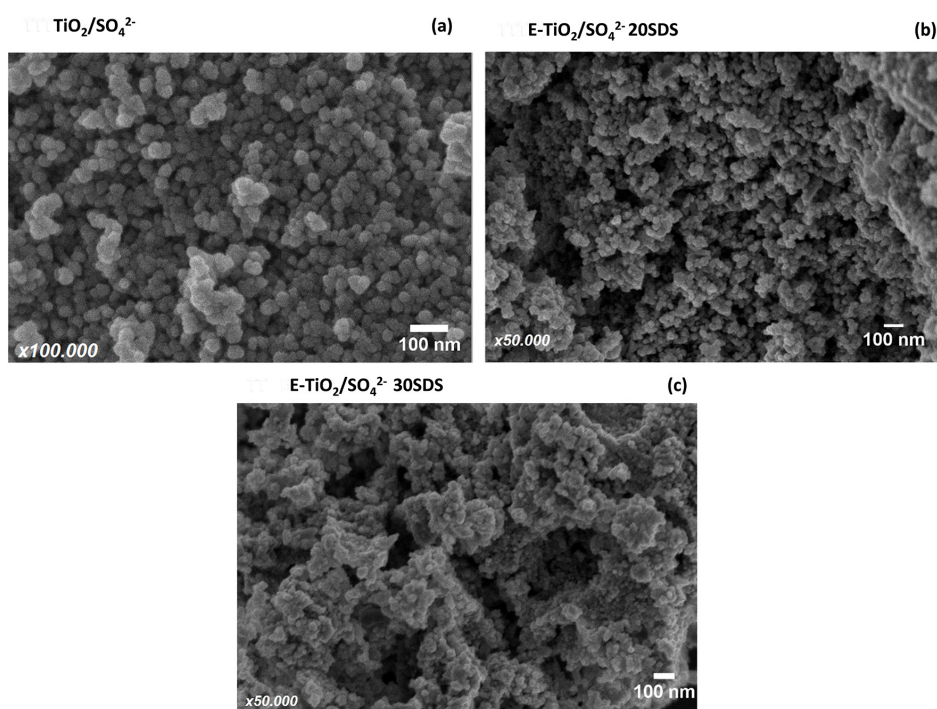
Figure 5. SEM images of non-foamed sulfated titania ((a) TiO$_2$/SO$_4^{2-}$), and sulfated titania foamed with 20% ((b) E-TiO$_2$/SO$_4^{2-}$ 20SDS) and 30% ((c) E-TiO$_2$/SO$_4^{2-}$ 30SD) of SDS.
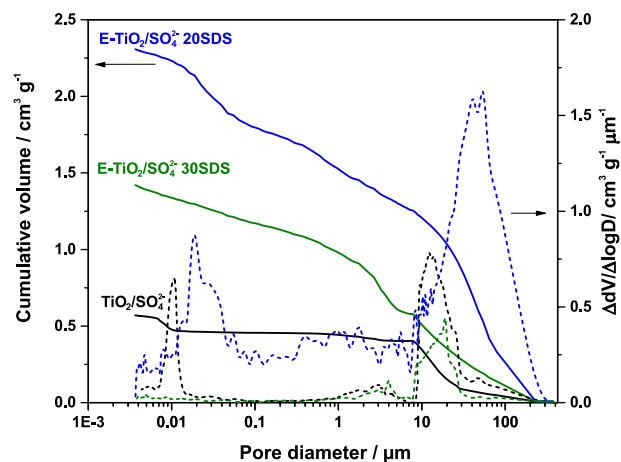
with the porous templated by the lamellar mesophase revealed by SAXS (Figure 4).

The cumulative pore size distributions from Hg intrusion (Figure 7) showed that the non-foamed sample exhibited a mesopores (size below 0.01 μm) and a macropores family. The mesopores were in agreement with the H1 hysteresis loop revealed by Figure 6, and their origin could be attributed to the smaller intra-agglomerate voids formed by primary titania particles bonded by the surface sulfate groups.[4,19,20] The macropores were originated from the inter-aggregate voids. This attribution is consistent with the considerable increase of the volume and average size of the larger macropores family for the sample foamed with 20% of SDS. In addition, the observed increases of mesopore volume and size indicated that the action of the SDS surfactant also affected the formation of the gel network and the resulting internal pores at the walls of the macropores. This hierarchical pore structure resulted in specific surface area and porosity as larger as those obtained for typical aerogels produced under supercritical conditions.[34] Increase of the SDS concentration to 30% favored densification of the macropore walls and the almost complete elimination of mesopores, with consequent shrinkage of the macropores and decrease of porosity and specific surface area. This behavior could be explained by higher stability of the mesophase, leading to structural coarsening by surface diffusion.[35]


Figure 7. Cumulative pore size distributions from Hg intrusion porosimetry analyses of the non-foamed (TiO$_2$/SO$_4^{2-}$) and foamed sulfated titania prepared using 20% (E-TiO$_2$/SO$_4^{2-}$ 20SDS) and 30% (E-TiO$_2$/SO$_4^{2-}$ 30SDS) of SDS.

shift the absorption towards the visible range, reducing the UV spectrum absorbance, due to the lower amount of Ti^{4+}.[37,38] This could explain the continuous band downshift caused by sulfation related to the addition of PTSH, for the non-foamed sample, and the combined addition of PTSH and SDS, in the case of the foamed sample.
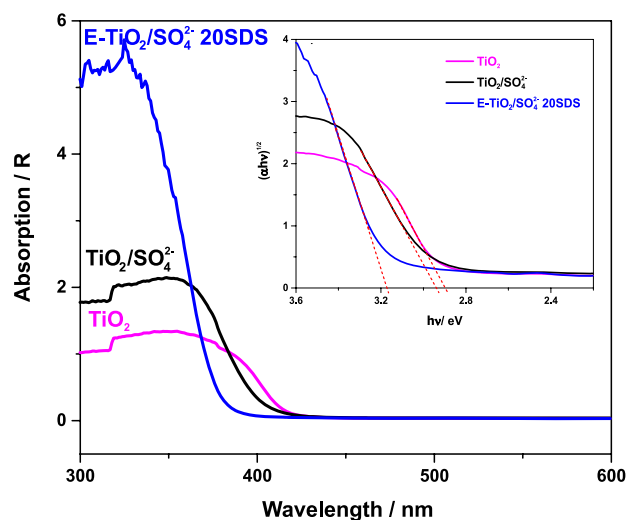
Figure 8. UV-Vis DRS spectra and Tauc plots (insert) for the indirect bandgap transition of non-foamed (TiO$_2$/SO$_4^{2-}$) and foamed (TiO$_2$/SO$_4^{2-}$ 20SDS) samples. The spectrum for titania (TiO$_2$) without SDS and sulfate is shown for comparison.

Figure 6. N$_2$ adsorption-desorption isotherms of the non-foamed (TiO$_2$/SO$_4^{2-}$) and foamed sulfated titania prepared using 20% (E-TiO$_2$/SO$_4^{2-}$ 20SDS) and 30% (E-TiO$_2$/SO$_4^{2-}$ 30SDS) of SDS.

UV-Vis DRS was used to investigate the optical properties of the non-foamed and foamed sulfated titania, with the resulting spectra (Figure 8) presenting absorption bands in the ranges 220-420 nm and 220-389 nm, respectively. These signals could be attributed to charge transfer from the valence band (VB), formed by 2p orbitals of O^{2-} anions, to the conduction band (CB), formed by 3d orbitals of Ti^{4+} cations.[16,36] It is well known that Ti^{3+} states

The Tauc plot of $(\alpha h\nu)^{1/2}$ *versus* photon energy, shown in the inset of Figure 8, enabled indirect determination of the bandgap energies by extrapolation of the linear regions of the curves to absorption equal to zero, resulting in values of 2.95 and 3.17 eV for the TiO$_2$/SO$_4^{2-}$ and TiO$_2$/SO$_4^{2-}$ 20SDS powders, respectively. The bandgap narrowing observed for the TiO$_2$/SO$_4^{2-}$ sample could be explained by the presence of Ti^{3+} defects,[38] while the 3.17 eV value for the

J. Braz. Chem. Soc. **2024**, *35*, 11, e-20240088

7 of 10

Table 2. Structural characteristics of non-foamed and foamed sulfated titania

Sample	Crystallite size / nm	E_g / eV	Macropores volume / (cm³ g⁻¹)	Average macropores size / μm	Total pores volume / (cm³ g)	Porosity / %	Surface area / (m² g⁻¹)
TiO_2/SO_4^{2-}	10	2.95	0.39	12	0.56	85	42
$E\text{-}TiO_2/SO_4^{2-}$ 20SDS	12	3.17	1.8	56	2.3	93	80
$E\text{-}TiO_2/SO_4^{2-}$ 30SDS	10	3.20	1.2	40	1.4	90	51

E_g: bandgap energy.

TiO_2/SO_4^{2-} 20SDS sample was in good agreement with the E_g value reported for the anatase phase of titania.[38-40]
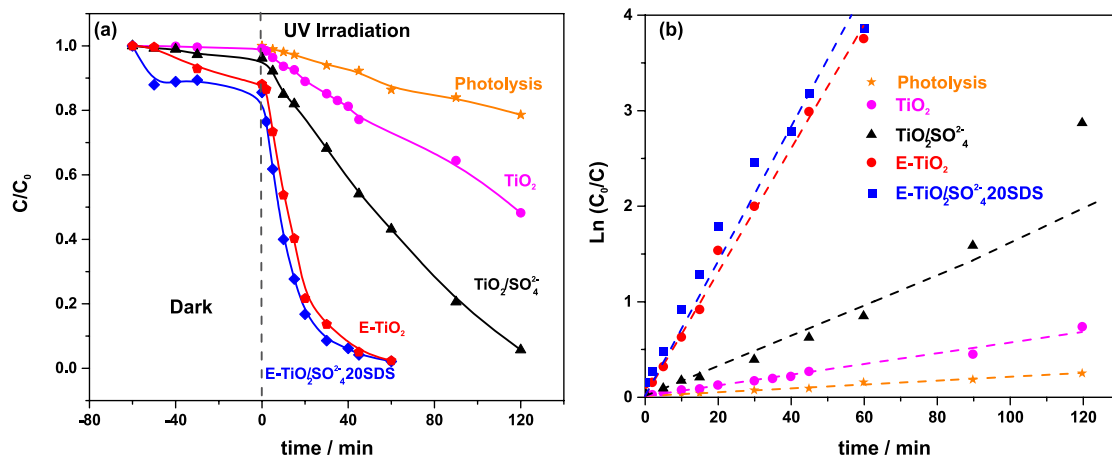
The photocatalytic activities of the titania foams applied in the RhB degradation reaction are shown in Figure 9. For comparison, it is also shown the photodegradation curve obtained for direct dye photolysis, under the same experimental conditions, but in the absence of a photocatalyst, which resulted in around 20% degradation after 120 min of irradiation (Figure 9a). Prior to UV light irradiation, the solutions containing the photocatalysts were stirred under dark conditions for 60 min, to ensure that adsorption of the dye on the photocatalysts reached equilibrium. In this step, the concentration of the dye solution decreased, with the decrease being greatest in the presence of the $E\text{-}TiO_2/SO_4^{2-}$ 20SDS foam, indicating a higher degree of adsorption, which could be explained by the fact that this material had the highest surface area (Table 2) and the presence of both Lewis and Brønsted acid sites. Since Rhodamine B is a cationic dye, electrostatic interaction between the dye molecules and the Brønsted acid sites could increase the adsorption on the titania surface modified with SO_4^{2-}. Analogous behavior was observed in studies of the photodegradation of Rhodamine, Methylene Blue, and phenol dyes adsorbed onto sulfated and non-sulfated TiO_2 photocatalysts.[3,36,40]

The degradation of RhB using the TiO_2/SO_4^{2-} 20SDS foam reached almost 100% at 60 min, while use of the non-foamed TiO_2/SO_4^{2-} resulted in only 94% RhB degradation after 120 min of reaction. The photodegradation kinetics was studied assuming a pseudo-first order process, described by the equation: $\ln(C_0/C_t) = kt$, where t is the time of reaction and k is the apparent rate constant. The fits and the kinetic parameters are shown in Figure 9b and Table 3, respectively. The good linearity of the curves confirmed that the kinetics of photodegradation of RhB followed a pseudo-first order mechanism. The highest photocatalytic activity was observed for the $E\text{-}TiO_2/SO_4^{2-}$ 20SDS foam, which presented the highest adsorption capacity and provided the highest k value and the shortest half-life time (Table 3).

Table 3. Apparent constant rate k, half-life times ($t_{0.5}$) and linear correlation coefficients (R^2) for the photodegradation reaction of RhB using the non-foamed and foamed sulfated titania

Photocatalyst	k / min⁻¹	R^2	$t_{0.5}$ / min
TiO_2/SO_4^{2-}	0.01581 ± 0.00074	0.98277	52
$E\text{-}TiO_2/SO_4^{2-}$ 20%SDS	0.07055 ± 0.00262	0.98637	11

The superior performance of the $E\text{-}TiO_2/SO_4^{2-}$ 20SDS foam could be attributed to the porous structure and greater surface area of this material, as well as the presence of

Figure 9. Comparison of the photocatalytic activities of the titania samples: (a) variation of RhB concentration, as function of irradiation time; (b) pseudo-first order plots of the photodegradation reactions.

surface sulfate groups, since a hierarchical porous structure and a high surface area favor the diffusion of reagents and products, as well as the diffusion and separation of the photoexcited charge carriers. The presence of SO_4^{2-} on the TiO₂ surface itself acts as efficient electron trapping centers by enhancing its activity.[16,36] Furthermore, the inductive effect of electrons related to the presence of the sulfate groups could also lead to more effective charge separation, favoring greater generation of reactive species, such as hydroxyl (•OH) and superoxide ($O_2^{•-}$) radicals.[40-42] In addition, taking account for the environmental application, hierarchically structured titania photocatalysts proved to be efficient to the removal of contaminants of natural, manufactured or chemical origin, including pharmaceutical and personal care products as well as endocrine-disrupting compounds, that pose a risk to the biota or humans.[5] Therefore, the hierarchical porous structure and higher active surface area, associated with the sulfate species, generated a synergic effect and improved the photocatalytic efficiency of the sulfated titania foams.

Conclusions

A method was successfully developed for the synthesis of sulfated TiO₂ foams by the integration of a sol-gel process with the use of an emulsion template. The one-step method represents a technological advance in techniques for the incorporation of sulfate on ceramic oxide, since it eliminates the impregnation step, while the emulsion template allows the synthesis of highly textured materials with hierarchical porous structures consisting of macro- and mesopores. The results confirmed effective metastabilization of the anatase crystalline phase by the surface modification with sulfate, resulting in a smaller crystallite size and larger surface area. Therefore, superior photocatalytic activity of the porous sulfated titania in the degradation of RhB dye was achieved. The TiO₂/SO_4^{2-} foam photocatalysts provided higher reaction rate constants and shorter reaction half-life times, indicating the synergic effect of the combination of larger surface area, hierarchical porous structure, and electron inductive effect caused by the SO_4^{2-} groups. Therefore, this approach constitutes a novel strategy for the preparation of high-performance TiO₂ photocatalysts.

Acknowledgments

References

1. Eddy, D. R.; Permana, M. D.; Sakti, L. K.; Sheha, G. A. N.; Solihudin, H. S.; Takei, T.; Kumada, N.; Rahayu, I.; *Nanomaterials* **2023**, *13*, 704. [Crossref]

2. Ma, Y.; Wang, X.; Jia, Y.; Chen, X.; Han, H.; Li, C.; *Chem. Rev.* **2014**, *114*, 9987. [Crossref]

3. Periyat, P.; Pillai, S. C.; McCormack, D. E.; Colreavy, J.; Hinder, S. J.; *J. Phys. Chem. C* **2008**, *112*, 7644. [Crossref]

4. Sowards, K.; Medina, H.; *App. Mater. Today* **2023**, *35*, 101962. [Crossref]

5. Rahman, N. A.; Chong, C. E.; Pichiah, S.; Nah, I. W.; Kim, J. R.; Oh, S.; Yoon, Y.; Vhoi, E. H.; Jang, M.; *Sep. Pur. Technol.* **2023**, *304*, 122294. [Crossref]

6. Ibhadon, A. O.; Fitzpatrick, P.; *Catalysts* **2013**, *3*, 189. [Crossref]

7. Fujishima, A.; Zhang, X.; Tryk, D. A.; *Surf. Sci. Rep.* **2008**, *63*, 515. [Crossref]

8. Rashid, R.; Shafiq, I.; Gilani, M. R. H. S.; Maaz, M.; Akhter, P.; Hussain, M.; Jeong, K.; Kwon, E. E.; Bae, S.; Park, Y.; *Chemosphere* **2024**, *349*, 140703. [Crossref]

9. Bento, R. T.; Correa, O. V.; Pillis, M. F.; *J. Eur. Ceram. Soc.* **2019**, *39*, 3498. [Crossref]

10. Nakajima, A.; Nakamura, A.; Arimitsu, N.; Kameshima, Y.; Okada, K.; *Thin Solid Films* **2008**, *516*, 6392. [Crossref]

11. Devi, L. G.; Kavitha, R.; *Mater. Chem. Phys.* **2014**, *143*, 1308. [Crossref]

12. Nishikiori, H.; Hayashibe, M.; Fujii, T.; *Catalysts* **2013**, *3*, 363. [Crossref]

13. Jothivel, S.; Velmurugan, R.; Selvam, K.; Krishnakumar, B.; Swaminathan, M.; *Sep. Pur. Technol.* **2011**, *77*, 245. [Crossref]

14. Parida, K. M.; Sahu, N.; Biswal, N. R.; Naik, B.; Pradhan, A. C.; *J. Colloid Interface Sci.* **2008**, *318*, 231. [Crossref]

15. Topalian, Z.; Stefanov, B. I.; Granqvist, C. G.; Osterlund, L.; *J. Catal.* **2013**, *307*, 265. [Crossref]

16. Lin, X. H.; Li, S. F. Y.; *Appl. Catal., B* **2015**, *170-171*, 263. [Crossref]

17. Zhang, H.; Yu, H.; Zheng, A.; Li, S.; Shen, W.; Deng, F.; *Environ. Sci. Technol.* **2008**, *42*, 5316. [Crossref]

18. Jin, T.; Yamaguchi, T.; Tanabe, K.; *J. Phys. Chem.* **1986**, *90*, 4794. [Crossref]

19. Lins, R. F.; Alves-Rosa, M. A.; Pulcinelli, S. H.; Santilli, C. V.; *J. Sol-Gel Sci. Technol.* **2012**, *63*, 224. [Crossref]

20. Martins, L.; Alves-Rosa, M. A.; Pulcinelli, S. H.; Santilli, C. V.; *Microporous Mesoporous Mater.* **2010**, *132*, 268. [Crossref]

J. Braz. Chem. Soc. **2024**, *35*, 11, e-20240088

9 of 10

21. Kaminski, R. C. K.; Pulcinelli, S. H.; Santilli, C. V.; Meneau, F.; Blanchandin, S.; Briois, V.; *J. Eur. Ceram. Soc.* **2010**, *30*, 193. [Crossref]

22. Cullity, B. D.; *Elements of X-Ray Diffraction*, 2nd ed.; Addison-Wesley Publishing Company Inc.: USA, 1978.

23. Nobbs, J. H.; Kubelka-Munk, P.; *Rev. Prog. Color. Relat. Top.* **1985**, *15*, 66. [Crossref]

24. Kubelka, P.; *J. Opt. Soc. Am.* **1948**, *38*, 448. [Crossref]

25. Yaghmur, A.; de Campo, L.; Salentinig, S.; Sagalowicz, L.; Leser, M. E.; Glatter, O.; *Langmuir* **2006**, *22*, 517. [Crossref]

26. Gregg, S. J.; Sing, K. S. W.; *Adsorption, Surface Area and Porosity*, 2nd ed.; Academic Press: London, UK, 1997.

27. Washburn, E. W.; *Phys. Rev.* **1921**, *17*, 273. [Crossref]

28. Lee, H. L.; Cheng, Y. S.; Yeh, K. L.; Lee, T.; *ACS Omega* **2021**, *6*, 15770. [Crossref]

29. Scolan, E.; Sanchez, C.; *Chem. Mater.* **1998**, *10*, 3217. [Crossref]

30. Lin, X. H.; Yin, X. J.; Liu, J. Y.; Li, S. F. Y.; *Appl. Catal., B* **2017**, *203*, 731. [Crossref]

31. Soni, S. S.; Brotons, G.; Bellour, M.; Narayanan, T.; Gibaud, A.; *J. Phys. Chem. B* **2006**, *110*, 15157. [Crossref]

32. Ramos, L.; Fabre, P.; *Langmuir* **1977**, *13*, 682. [Crossref]

33. Manaia, E. B.; Kaminski, R. C. K.; Soares, C. P.; Meneau, F.; Pulcinelli, S. H.; Santilli, C. V.; Chiavacci, L. A.; *J. Sol-Gel Sci. Technol.* **2012**, *63*, 251. [Crossref]

34. Kistler, S. S.; *Nature* **1931**, *127*, 741. [Crossref]

35. Kaminski, R. C. K.; Pulcinelli, S. H.; Judeinstein, P.; Meneau, F.; Briois, V.; Santilli, C. V.; *J. Phys. Chem. C* **2010**, *114*, 1416. [Crossref]

36. Devi, L. G.; Aruna, M. L. K.; *J. Mol. Catal. A: Chem.* **2014**, *391*, 99. [Crossref]

37. Manzo-Robledo, A.; López, A. C.; Caballero, A. A. F.; Cadena, A. A. Z.; López, M.; Vázquez-Cuchillo, O.; *Mater. Sci. Semicond. Process.* **2015**, *31*, 94. [Crossref]

38. Nursam, N. M.; Wang, X.; Tan, J. Z. Y.; Caruso, R. A.; *Appl. Mater. Interfaces* **2016**, *8*, 17194. [Crossref]

39. Lee, H. S.; Woo, C. S.; Youn, B. K.; Kim, S. Y.; Oh, S. T.; Sung, Y. E.; Lee, H. I.; *Top. Catal.* **2005**, *35*, 255. [Crossref]

40. Colon, G.; Hidalgo, M. C.; Navio, J. A.; *App. Catal., B* **2003**, *45*, 39. [Crossref]

41. Chen, L.; Yang, S.; Mäder, E.; Ma, P.; *Dalton Trans.* **2014**, *43*, 12743. [Crossref]

42. Xie, C.; Yang, Q.; Xu, Z.; Du, Y.; *J. Mol. Catal. A: Chem.* **2014**, *381*, 107. [Crossref]